Journal of
Materials Chemistry A
Materials for energy and sustainability

This article can be cited before page numbers have been issued, to do this please use: T. Yang, E. Boutelle, M. Efroza, P. Zhang and P. Bai, *J. Mater. Chem. A*, 2026, DOI: 10.1039/D6TA03125K.

Volume 6
Number 12
28 March 2018
Pages 4883-5230

Journal of
Materials Chemistry A
Materials for energy and sustainability
rsc.li/materials-a

ISSN 2050-7488

ROYAL SOCIETY
OF CHEMISTRY

COMMUNICATION
Zhenhai Wen *et al.*
An electrochemically neutralized energy-assisted low-cost acid-alkaline electrolyzer for energy-saving electrolysis hydrogen generation

ROYAL SOCIETY
OF CHEMISTRY

rsc.li/materials-a

View Article Online
DOI: 10.1039/D6TA03125K

Surface modification enables long-term cycling of Prussian white in sodium-ion batteries

Tingting Yang[a], Ethan Boutelle[a], Maurice Efroza[b], Penghao Zhang[a], Peng Bai[a,b,*].

[a]Department of Energy, Environmental and Chemical Engineering, Washington University in St. Louis, St. Louis, Missouri 63130, United States of America

[b]Institute of Materials Science and Engineering, Washington University in St. Louis, St. Louis, Missouri 63130, United States of America

Corresponding Author: Peng Bai

Email: pbai@wustl.edu

View Article Online
DOI: 10.1039/D6TA03125K

Abstract: Prussian blue analogs (PBAs) are promising cathodes for sodium-ion batteries. Yet, their cycling stability is limited by intrinsic structural degradation and surface deterioration associated with the open metal–CN coordination network. Here, we present a synergistic strategy combining particle-level surface modification and electrode-level additive dispersion to enhance the performance and durability of manganese hexacyanoferrate. The controlled addition of ammonium persulfate forms a reconstructed surface layer that stabilizes the open framework during ion (de)intercalation. Acid-treated carbon (ATC) dispersed in the precursor improves nucleation during synthesis, as well as the electronic conductivity and charge transfer during electrode operation. The resulting PBA microcubes show excellent durability, sustaining stable cycling for 500 cycles at 1C. The feasibility of this approach was further demonstrated in a scaling-up attempt with higher reactant concentrations. The optimized PBA material delivers a high specific capacity of 140 mA·h·g^{-1} at 0.1C, along with excellent rate capability, retaining 108.6 mA·h·g^{-1} even at 10C.

View Article Online
DOI: 10.1039/D6TA03125K

1. Introduction

Prussian blue analogs (PBAs) have attracted extensive attention as promising cathode materials for sustainable sodium-ion batteries (SIBs), owing to their facile and low-cost synthesis.[1-3] Their open framework ensures efficient Na^+ kinetics and accommodates volume changes during cycling, which are essential for stable electrochemical performance.[4-6] Among the various PBAs, manganese hexacyanoferrate (MnHCF), often referred to as a Prussian White material, has emerged as a leading candidate for high-energy-density SIBs.[7, 8] MnHCF has a high theoretical capacity of ~170 $mA{\cdot}h{\cdot}g^{-1}$ at the potential of ~3.5 V versus Na/Na^+.[9, 10] Its chemical formula can be expressed as $Na_2Mn[Fe(CN)_6]_y\square_{1-y}{\cdot}nH_2O$ ($0 < y \leq 1$), where □ denotes ferricyanide vacancies. The MnHCF crystals adopt a double perovskite framework composed of interconnected MnN_6 and FeC_6 octahedra, with Na^+ ions and water molecules occupying the interstitial sites.[11, 12]

Although the open framework of MnHCF provides abundant interstitial sites for easy Na^+ ion insertion and extraction, its long-term cycling stability remains lower than expected, which can be attributed to several intrinsic and extrinsic factors. MnHCF is typically synthesized via a simple coprecipitation reaction between Mn^{2+} ions and $[Fe(CN)_6]^{4-}$ anions in an aqueous solution. This rapid precipitation process often results in structural defects, particularly a high concentration of ferricyanide vacancies, which destabilize the framework and undermine the cycling performance.[13-15] Furthermore, the aqueous synthesis condition leads to residual water in the final crystal structure, which may even reach 20 wt% of the total mass of materials.[16, 17] The presence of interstitial water molecules not only reduces the number of available Na^+ storage sites but also blocks the ion diffusion channels, thereby hindering fast Na^+ transport. When not engineered properly, some particles in the porous electrode may experience over-oxidation of $[Fe(CN)_6]^{4-}$ units and release cyanide-derived species (CN^-, $(CN)_2$, cyanogen), which chemically attack electrolyte molecules and trigger gas evolution.[18, 19] Unstable surface sites also accelerate the dissolution of redox-active transition metals into the electrolyte.[20, 21]

To mitigate these issues, Galceran et al. investigated the dehydration and rehydration

View Article Online
DOI: 10.1039/D6TA03125K

process of $Na_{1.87}Mn[Fe(CN)_6]_{0.99}\cdot 1.99H_2O$, demonstrating that a high-performance dehydrated rhombohedral phase can be achieved by vacuum drying at 150 °C and 20 mbar for 20 h, where temperature and pressure enable a synergistic effect on phase formation.[9] Wu et al. reported that heating Prussian White materials at 180 °C induces a phase transition from monoclinic to rhombohedral, leading to lattice contraction and reduced water content.[17] The use of chelating agents such as ethylenediaminetetraacetic acid (EDTA) and trisodium citrate during coprecipitation can regulate the nucleation and growth rates and effectively reduce the number of $[Fe(CN)_6]^{4-}$ vacancies.[22-24] In the effort of improving the particle surfaces, in-situ polymerization of organic polymer monomers such as pyrrolidone was reported as an effective strategy to alleviate interfacial side reactions. [25, 26] Fu et al. further developed a chemically regulated hollow core-shell structure composed of manganese-based cores and iron-based shells (Mn@Fe/H-PBA), in which the synergistic Fe^{2+}/Fe^{3+} and Mn^{2+}/Mn^{3+} redox couples deliver high specific capacity and improved Na^+ storage capability. [27] In addition, a high-entropy strategy has been employed to stabilize Mn-based Prussian blue analogues by introducing equimolar Fe, Co, Ni, and Cu into the Mn sites, thereby activating otherwise inert Fe sites. The resulting HE-Mn-PBA exhibits enhanced specific capacity and prolonged cycling stability in aqueous sodium-ion batteries. [28]

In this work, we propose a simple one-pot one-step but synergistic approach to achieve high-performance MnHCF. The synthesis is conducted in aqueous solutions with uniformly dispersed acid-treated carbon, triggering more uniform nucleation during coprecipitation and ensuring intimate electrical contact between the MnHCF microcubes and enhancing charge transport and transfer in the final electrode. In the meantime, the surface modification by the controlled addition of low-concentration ammonium persulfate partially oxidized low-spin Fe^{2+} into Fe^{3+} ions, forming the NH_4^+ and Fe^{3+} enriched surface layer to stabilize the open framework during redox reactions while simultaneously mitigating electrolyte attack. Benefiting from these synergistic modifications, our material exhibits a much prolonged cycling lifespan in sodium-ion half-cells. Our work provides new insights into the role of surface engineering in advancing Prussian White cathode materials.

View Article Online
DOI: 10.1039/D6TA03125K

2. Results and discussion

2.1 Design strategy and structural integrity of surface-modified MnHCF microcubes

Pristine manganese hexacyanoferrate, denoted as MnHCF-0, was synthesized using the slow coprecipitation synthesis method[14] with the help of ascorbic acid under an ice bath and nitrogen protection. To stabilize the electrode/electrolyte interface of MnHCF without sacrificing its bulk crystal framework, a combined surface engineering strategy involving acid-treated carbon (ATC) incorporation and mild ammonium persulfate (APS) oxidation was developed. As illustrated in Figure 1(a) and detailed in the Experimental Section. A certain amount of ATC was uniformly dispersed in the HPLC-grade water in an ultrasonic bath. Afterward, a certain mass of $Na_2MnC_{10}H_{12}N_2O_8$ ($Na_2MnEDTA$) and $Na_4Fe(CN)_6 \cdot 10H_2O$ were added to the ATC solution to prepare the reactant solution. Subsequently, the ascorbic acid solution was gradually added to the reactant solution, thereby inducing the dissociation reaction and triggering the precipitation of manganese hexacyanoferrate. After aging, 0.01, 0.03, and 0.05 mol L^{-1} of $(NH_4)_2S_2O_8$ solution (APS) was slowly added into the reactor, respectively, to produce ATC/MnHCF-1, ATC/MnHCF-3, and ATC/MnHCF-5. The concentration of APS solution was carefully controlled to create an appropriate thickness of the protective surface layer. This design aims to induce moderate surface oxidation and interfacial reconstruction while preserving the bulk phase and morphology of the Prussian White microcubes.

The structural integrity and morphological features of the as-prepared samples were first examined to verify that the surface treatment does not disrupt the bulk framework. Scanning electron microscopy (SEM) images of four samples are shown in Figure 1(b–e) and Figure S1. Figure 1(b) reveals that MnHCF-0 are reunited cubes with a size of 3–5 μm. All ATC/MnHCF-1, ATC/MnHCF-3, and ATC/MnHCF-5 cubes are of a similar size. Figure 1(d) displays the uniform distribution of carbon particles and microcubes of ATC/MnHCF-3. ATC additives obviously reduced the agglomeration of Prussian White cubes. Compared with pristine MnHCF-0, ATC/MnHCF-3 shows a

View Article Online
DOI: 10.1039/D6TA03125K

rougher surface, as shown in the enlarged Figure 1(e), implying mild surface etching and oxidation. Moreover, elements Na, Mn, Fe, and N are evenly distributed in the single cube as revealed by Energy Dispersive Spectroscopy (EDS) mapping images. The EDS elemental line-scan distribution maps for the cubic particles in both the MnHCF-0 and ATC/MnHCF-3 samples are illustrated in Figure S2, which also elucidate the homogeneous distribution of elements along the selected scan direction. Inductively Coupled Plasma Mass Spectrometry (ICP-MS) and Thermogravimetric analysis (TGA) were employed to quantify the chemical composition and water content of synthesized manganese hexacyanoferrate. The detailed results are shown in Table S1 and Figure S3. The content of water in synthesized samples is reduced largely from 12wt% to approximately 6wt% based on the calculation of weight loss at 230 °C. By combining the ICP-MS and TGA results, the chemical formula of MnHCF-0, ATC/MnHCF-1, ATC/MnHCF-3, and ATC/MnHCF-5, after enforcing electroneutrality, are $Na_{1.80}Mn[Fe(CN)_6]_{0.95}\square_{0.05}\cdot 2.26H_2O$, $Na_{1.93}Mn[Fe(CN)_6]_{0.98}\square_{0.02}\cdot 0.53H_2O$, $Na_{1.47}Mn[Fe(CN)_6]_{0.8}\square_{0.13}\cdot 0.97H_2O$, and $Na_{1.27}Mn[Fe(CN)_6]_{0.82}\square_{0.18}\cdot 0.60H_2O$. According to the above stoichiometric ratios, the sodium ion content decreases with increasing ammonium persulfate concentration, which can be attributed to the slightly increased valence of transition metal elements caused by the oxidation reaction of ammonium persulfate.

View Article Online
DOI: 10.1039/D6TA03125K

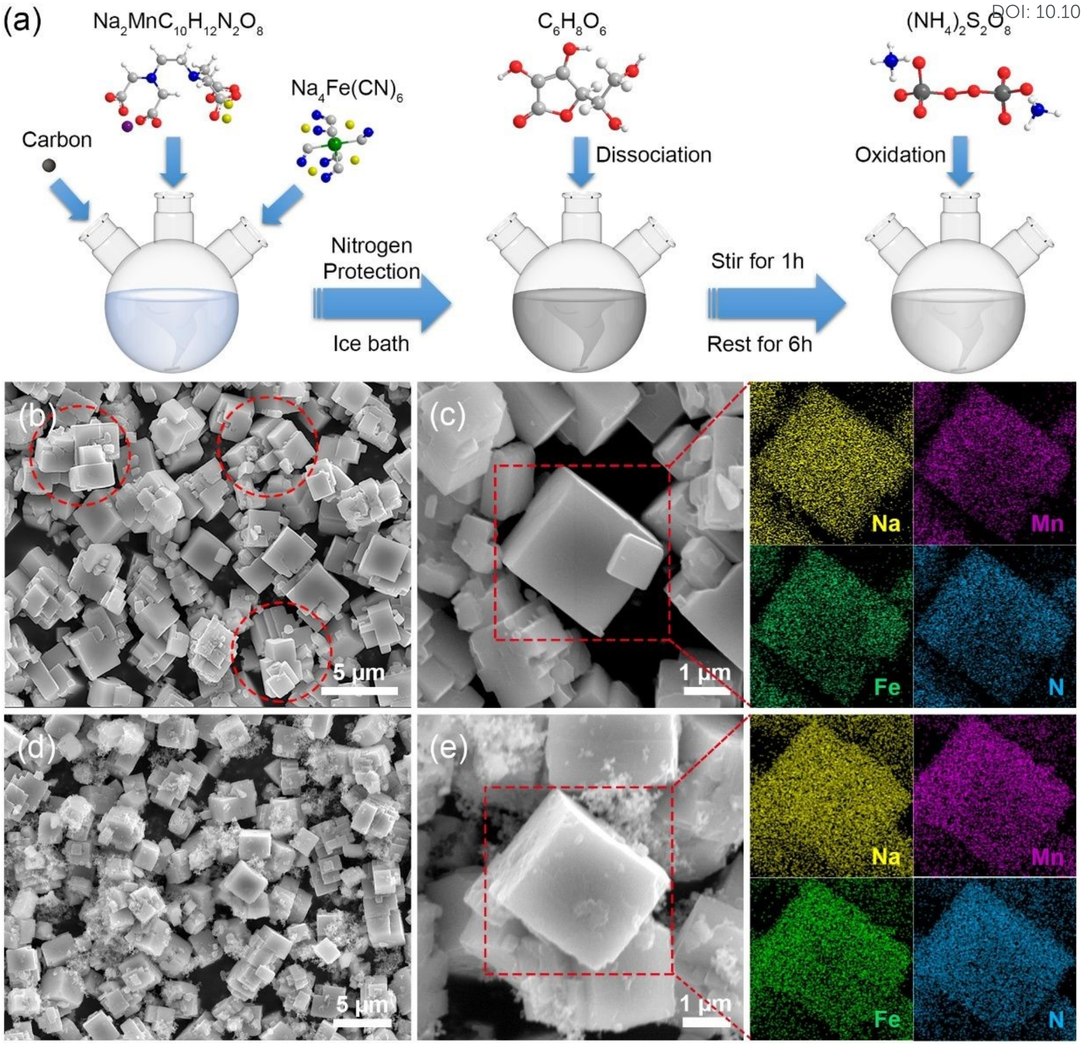

Figure 1 (a) Illustration of the synthesis procedure of treated manganese hexacyanoferrate by using the coprecipitation method. SEM images and corresponding EDS mapping images of (b, c) MnHCF-0 and (d, e) ATC/MnHCF-3.

Powder X-ray diffraction (XRD) patterns of MnHCF-0, ATC/MnHCF-1, ATC/MnHCF-3, and ATC/MnHCF-5 are displayed in Figure 2(a). The peaks in four patterns can be indexed to two crystal structures, which are the dehydrated rhombohedral (JCPDS PDF card#00-067-0177) and hydrated monoclinic (JCPDS PDF card#00-067-0176).[29, 30] Both rhombohedral and monoclinic phases can accommodate enough Na^+ ions for redox reaction. Rietveld refinements in Figure 2(b) and Figure S4 show that MnHCF-0 is composed with 81.55% of rhombohedral and 18.45% of monoclinic phases. The fraction of the monoclinic phase was increased slightly with the more concentrated APS solution. The rhombohedral structure has the space group

View Article Online
DOI: 10.1039/D6TA03125K

of $R\bar{}-3$ ($a = b = 6.586(9)$ Å, $c = 18.84(5)$ Å, $\alpha = \beta = 90°$, $\gamma = 120°$), while the monoclinic phase shows the $P2_1/n$ space group ($a = 10.58(2)$ Å, $b = 7.46(3)$ Å, $c = 7.35(2)$ Å, $\alpha = \gamma = 90°$, $\beta = 91.8(2)°$) (Figure 2(c)).[31] With the increase of APS concentration, the lattice constants of treated MnHCF show a clear decreasing trend (Tables S2-3), where ATC/MnHCF-3 exhibits the smallest constants. This can be attributed to the oxidation of Fe^{2+} (0.61 Å) to smaller Fe^{3+} (0.55 Å). Fourier Transform Infrared Spectroscopy (FTIR) was applied to explore the bonding of species in the four synthesized materials. As shown in Figure 2(d), characteristic peaks at 451 cm^{-1} and 594 cm^{-1} are attributed to the bending and stretching vibration of the Fe—C bonds.[32] The peak at 2064 cm^{-1} can be assigned to the cyan bond stretching mode of $\upsilon(C\equiv N)$ in $[Fe(CN)_6]^{4-}$ ligands. Moreover, three characteristic transmission peaks at 1619 cm^{-1}, 3538 cm^{-1}, and 3609 cm^{-1} are associated with the bending or stretching mode of O—H of interstitial water, and the stretching mode of O—H of surface water.[9] In particular, a small peak at 1413 cm^{-1} appeared only in the modified materials, which is a signature of the bending vibration of N—H bonds,[33, 34] proving the existence of NH_4^+ ions in the open framework. Furthermore, Raman spectra are more sensitive to the stretching vibration of transition metals bonded with cyan groups, which are beneficial for further distinguishing transition metals in manganese hexacyanoferrate.[35] Figure 2(e) shows the Raman spectra between 1900 and 2300 cm^{-1}. With the increase of APS concentration, corresponding spectra show significant changes, reflecting the valence changes of transition metals. For pristine MnHCF-0, peaks at 2068 and 2092 cm^{-1} correspond to Fe^{II}—CN—Mn^{II} bonds, while the peak at 2131 cm^{-1} indicates Fe^{II}—CN—Mn^{III} bonds.[36] For ATC/MnHCF-3 and ATC/MnHCF-5, an additional peak appears at 2160 cm^{-1} indicates Fe^{III}—CN—Mn^{II} bonds.[36] The comparison of low wavenumber Raman spectra of MnHCF-0 and ATC/MnHCF-3 are shown in Figure S5. In the lower wavenumber region, the vibrational modes between 400 and 600 cm^{-1} in the spectrum of MnHCF-0 correspond to Fe–C stretching. In contrast, the Fe–C stretching vibrations of the ATC/MnHCF-3 sample shift to higher wavenumber region at 500–700 cm^{-1}, demonstrating the oxidation of iron ions.

View Article Online
DOI: 10.1039/D6TA03125K

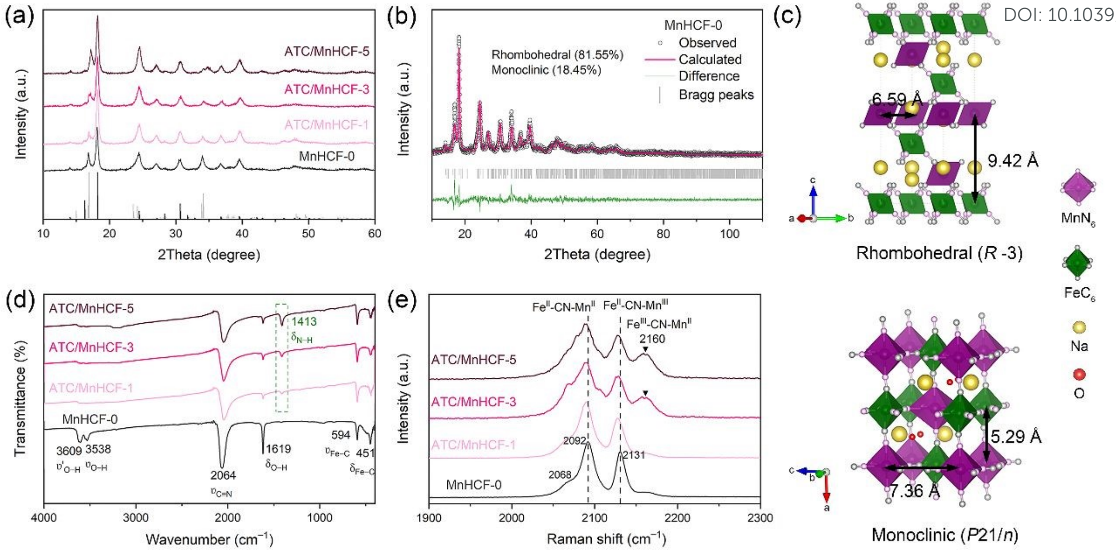

Figure 2 (a) XRD patterns of manganese hexacyanoferrate samples in a mixture of rhombohedral and monoclinic phases. (b) Rietveld refinement results of MnHCF-0 XRD data. (c) Illustrations of rhombohedral and monoclinic crystal structures. (d) FTIR spectra, and (e) Raman spectra of MnHCF-0, ATC/MnHCF-1, ATC/MnHCF-3, and ATC/MnHCF-5.

2.2 Surface chemical state regulation via mild oxidative treatment

To directly verify the surface-localized nature of the oxidation and to elucidate the resulting valence-state distribution, X-ray photoelectron spectroscopy (XPS) combined with Ar^+ sputtering was employed to probe the near-surface chemical states of Fe and Mn in MnHCF-0, ATC/MnHCF-1, ATC/MnHCF-3, and ATC/MnHCF-5. As shown in Figure 3(a–d), XPS spectra of Fe 2*p* for each sample were collected after three-minute sputtering for a total time of fifteen minutes, to detect about tens of nanometers deep of Prussian White materials' surface. All XPS spectra were calibrated based on the C 1*s* peak at 284.8 eV. The first set of spectra, without sputtering, exhibited a peak at 709 eV (Fe^{III} $2p_{3/2}$),[37] which is expected even for the pristine MnHCF, as the air exposure can also oxidize the Fe^{II}. The sputtering is necessary and indeed reveals different chemical features. The primary single peak at 709 eV is split into two peaks, and one is shifted to lower binding energy, demonstrating a clear valence gradient from surface to bulk. To quantitatively compare the iron valence states of four samples, we fitted and

View Article Online
DOI: 10.1039/D6TA03125K

deconvoluted the spectra obtained after fifteen minutes of sputtering, as shown in Figure 3(e–h). Two peaks at approximately 708 eV and 709 eV correspond to Fe^{II} $2p_{3/2}$ and Fe^{III} $2p_{3/2}$, respectively. [38] Among the four samples, the relative amount of Fe^{III} is gradually increased, from 73 at% (MnHCF-0) to 79 at% (ATC/MnHCF-3) and finally 81.3 at% (ATC/MnHCF-5). It is concluded that the relative content of Fe^{3+} increases systematically with APS concentration, confirming that APS treatment effectively enriches Fe^{3+} species in the surface region. Furthermore, XPS spectra of Mn $2p$ for four samples are illustrated in Figure S6. All four Mn $2p$ spectra after fifteen minutes of sputtering showed two peaks at 642 eV and 656 eV, which are consistent with Mn^{II} $2p_{3/2}$ and Mn^{II} $2p_{1/2}$, respectively, verifying the bulk valence of Mn is +2 in four samples.[38, 39] Therefore, the oxidation reaction predominantly occurred at the Fe sites. Based on Fe $2p$ and Mn $2p$ XPS spectra of four samples, a core–shell–like chemical configuration can be proposed (Figure 3i), consisting of a Fe^{2+}-rich bulk and a Fe^{3+}/NH_4^+-enriched surface layer.

The incorporation of NH_4^+ is expected to suppress coordinated water formation and stabilize the framework. Besides, ex-situ Raman results of MnHCF-0 and ATC/MnHCF-5 electrodes under various cutoff voltages are displayed in Figure 3(j). The Raman spectra after charging have a single peak at a higher wavenumber, indicating the oxidation of Mn and Fe. However, their Raman spectra show some differences after discharging. The Raman spectrum of MnHCF-0 recovers to two peaks, which are consistent with the bonding of Fe^{II}—CN—Mn^{II} and Fe^{II}—CN—Mn^{III} at its initial state, while the Raman spectrum of ATC/MnHCF-5 shows a small shoulder at ~2130 cm^{-1}, indicating the bonds of Fe^{III}—CN—Mn^{II}. It is inferred that part of the surface Fe^{3+} species does not fully participate in the redox process, implying a structural stabilization role rather than an electrochemically active one. These observations collectively confirm that APS treatment constructs a chemically reconstructed surface passivation layer, which is designed to stabilize the crystal structure and mitigate surface degradation during repeated Na^+ insertion/extraction.

View Article Online
DOI: 10.1039/D6TA03125K

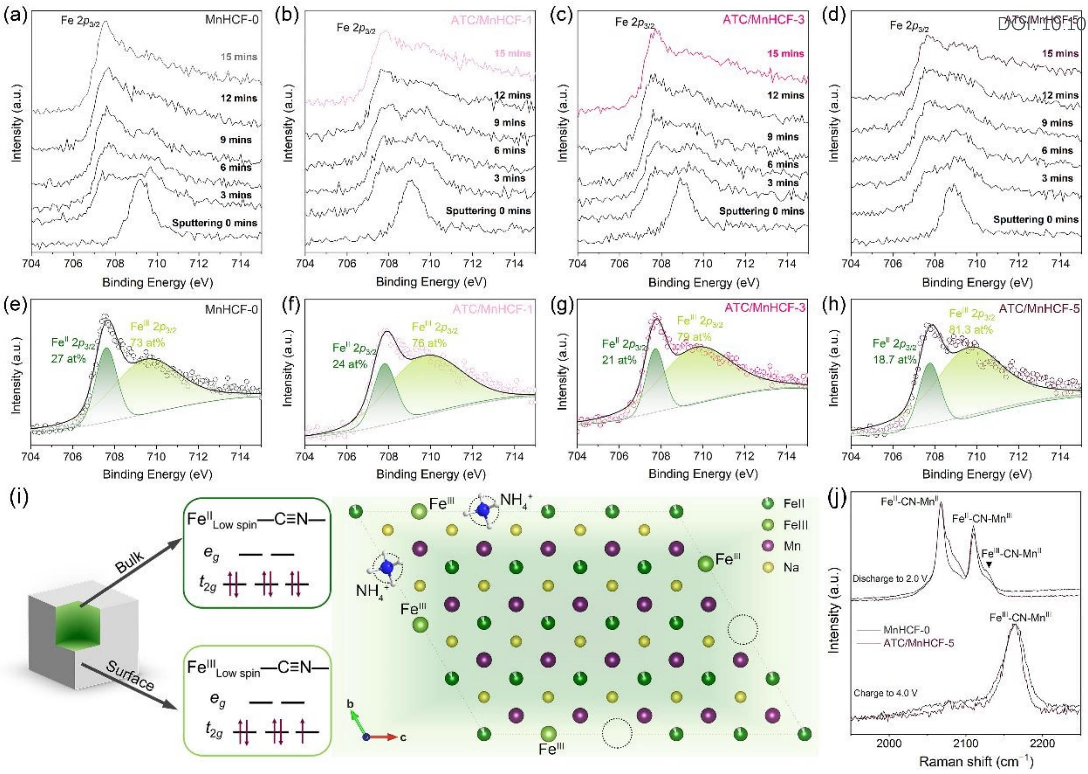

Figure 3 Fe 2*p* XPS spectra of MnHCF-0 (a, e), ATC/MnHCF-1 (b, f), ATC/MnHCF-3 (c, g), and ATC/MnHCF-5 (d, h) after different sputtering times. (i) Illustration of the iron valence distribution of ATC/MnHCF samples. (j) Ex-situ Raman spectra of MnHCF-0 and ATC/MnHCF-5 electrodes under various cutoff voltages.

2.3 Electrochemical performance of big particles

The electrochemical performance of MnHCF-0, ATC/MnHCF-1, ATC/MnHCF-3, and ATC/MnHCF-5 was systematically evaluated in sodium-ion half-cells. Figure 4(a) presents the Cyclic Voltammetry (CV) curves of all half-cells at the scan rate of 0.1 mV·s^{-1}. These CV curves show a single pair of redox peaks associated with the overlapping Mn^{2+}/Mn^{3+} and Fe^{2+}/Fe^{3+} redox couples,[40] indicating that the fundamental reaction mechanism remains unchanged after modification. The oxidation/reduction peaks of pristine MnHCF-0 are located at 3.61/3.32 V, corresponding to a voltage polarization of 0.29 V. In comparison, treated samples showed a decrease of voltage polarization to 0.21 V. Figure 4(b) shows the first charge and discharge curves of half-cells at 0.1C (1C = 150 mA·g^{-1}), with one pair of plateaus, which is the typical characteristic of the rhombohedral phase. The pristine MnHCF-0 big particles exhibit

View Article Online
DOI: 10.1039/D6TA03125K

a specific discharge capacity (124.7 mA·h·g^{-1}) with an initial coulombic efficiency of 79.3%. The rate performance of half-cells from 0.1C to 10C is shown in Figure 4(c). MnHCF-0 coin-cell delivered 124.4, 122.8, 118.5, 118.3, 111.8, 106.3, 96 mA·h·g^{-1} at 0.1C, 0.2C, 0.5C, 1C, 3C, 5C, and 10C, respectively. ATC/MnHCF-1 had the highest specific capacity of 110.6 mA·h·g^{-1} at 10C. The reduced voltage polarization and promoted rate performance can be ascribed to the improved electronic conductivity provided by the well-dispersed ATC network.

Furthermore, the long-term cycling tests of half-cells were conducted at both 1C and 3C, and their results are shown in Figure 4(d−f). The initial specific discharge capacities of MnHCF-0, ATC/MnHCF-1, ATC/MnHCF-3, ATC/MnHCF-5 were 126.2, 124.6, 120.5, and 112.7 mA·h·g^{-1} at 1C. After 500 cycles, the specific capacity of the MnHCF-0 cell decreased to 80.9 mA h g^{-1}, corresponding to the capacity retention of 64%. In contrast, ATC/MnHCF-3 showed the highest specific discharge capacity of 94.7 mA·h·g^{-1} after 500 cycles, achieving a capacity retention of up to 79%. Corresponding charge and discharge curves at various cycles can be found in Figure S7. Figure 4(d) displays the median charge/discharge voltages of MnHCF-0 and ATC/MnHCF-3 half-cells during their cycling at 1C. It can be observed that the overpotential of MnHCF-0 increased much more than that of the ATC/MnHCF-3 half-cell. In other words, the discharge energy density of MnHCF-0 decreased more than that of the ATC/MnHCF-3 half-cells. Conversely, the treated ATC/MnHCF-3 retains better energy density during long-term cycling. Half-cells with treated materials also showed better long-term cycling stability at 3C. ATC/MnHCF-3 achieved a capacity retention of 76% with the specific discharge capacity of 87.4 mA·h·g^{-1} after 1000 cycles at 3C, while the capacity retention of MnHCF-0 half-cell is only 61% after long-time cycling. To evaluate the reproducibility of the electrochemical performance, cycling tests were repeated using independently assembled cells, and the corresponding standard deviations were calculated. As shown in Figures S8 and S9, the standard deviation of the pristine MnHCF-0 sample ranges from 2–6%, whereas the modified samples exhibit smaller deviations of approximately 0–4%, indicating improved reproducibility and reduced cell-to-cell variation after surface modification. These additional data confirm

View Article Online
DOI: 10.1039/D6TA03125K

that the enhanced electrochemical performance of the modified materials is consistently observed across independently assembled cells. Therefore, the improved long-term stability can be attributed to the surface passivation method, which reduces the dissolution of transition metal ions and consequently ensures the reversible capacity. To sum up, the combination of surface modification and carbon incorporation has been shown to synergistically enhance the cycling stability and rate capability of Prussian White cathodes.

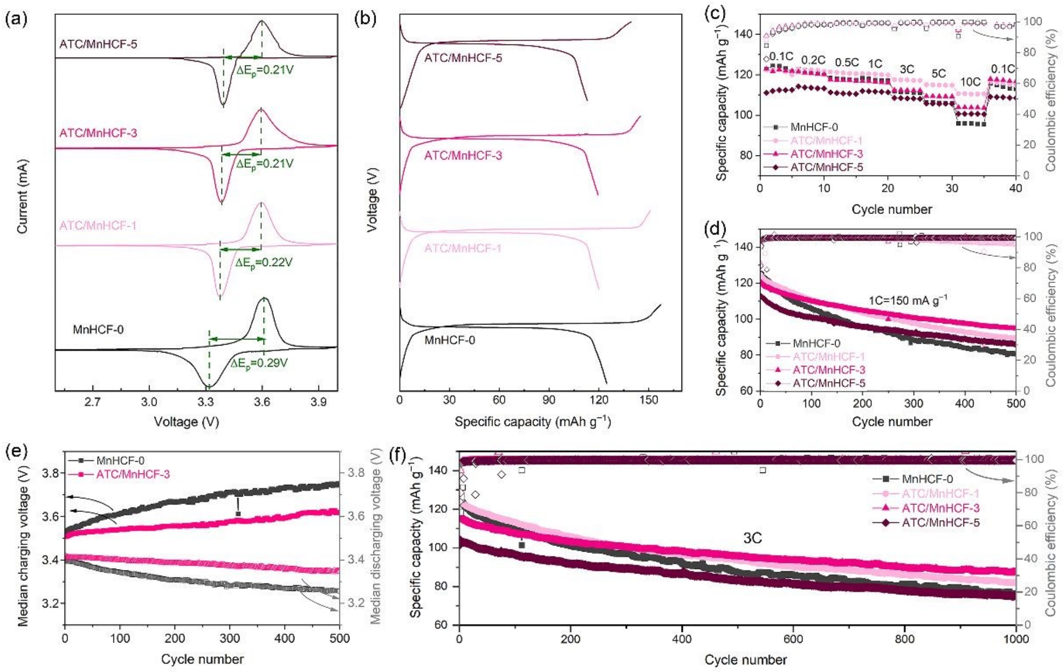

Figure 4 The electrochemical performance of MnHCF-0//Na, ATC/MnHCF-1//Na, ATC/MnHCF-3//Na, and ATC/MnHCF-5//Na half-cells. (a) CV curves at a scan rate of 0.1 $mV\cdot s^{-1}$. (b) Charge and discharge curves of the first cycle at 0.1C. (c) Rate performance from 0.1C to 10C. (d) Cycling performance at 1C and (d) corresponding median charge/discharge voltage profile. (f) Long-term cycling performance at 3C.

2.4 Mechanistic understanding of interfacial stabilization revealed by in-situ EIS and post-mortem characterization

Although the above electrochemical results demonstrate that surface modification markedly enhances the cycling stability of MnHCF, direct mechanistic evidence is still required to elucidate how the interfacial processes and charge-transport kinetics evolve during repeated Na^+ insertion/extraction. In-situ electrochemical impedance spectroscopy (EIS) provides a powerful means to monitor the frequency-dependent response of the cell during actual charge/discharge, enabling real-time tracking of multiple electrochemical processes across different time constants. MnHCF-0 and ATC/MnHCF-3 half-cells were cycled at 0.1C and Nyquist plots were taken at incremental one-hour intervals. As displayed in Figure 5(a, c), the semicircle at high frequencies reflects the charge transfer process, while the oblique at low frequencies is related to the Warburg diffusion process.[41] The first curve of the MnHCF-0 coin-cell showed a semicircle of 240 Ω, larger than that of ATC/MnHCF-3 (89 Ω), demonstrating the larger electron transfer impedance of the MnHCF-0 electrode. During the charge process, the electron transfer impedance of MnHCF-0 and ATC/MnHCF-3 coin-cells remained, while the tails in the low-frequency diffusion-controlled region gradually shifted to low angles with the extraction of Na^+ ions, manifesting the decrease of Na^+ ion diffusion rates.[42] During the discharge process, the charge transfer resistance of MnHCF-0 and ATC/MnHCF-3 coin-cells increased slightly, which can be assigned to the formation of the solid electrolyte interphase.

To further interpret the in-situ Nyquist curves and distinguish various processes, the distribution of relaxation time (DRT) analysis by modelling infinite parallel resistance (R) and capacitance (C) can be employed as a mathematical deconvolution method that transforms the impedance spectrum into a set of distinct peaks, each corresponding to a specific physical process with a characteristic timescale. In this way, DRT acts like a "spectral separator" that allows the complex impedance response to be intuitively decomposed into individual contributions, enabling a more quantitative and physically transparent comparison of the dynamic interfacial evolution of MnHCF-0 and ATC/MnHCF-3 electrodes. The contour plots of the DRT results in Figure 5 (b, d) display the relaxation time constant (τ) along the x-axis and the time variable along the y-axis, with the color scale and peak area reflecting the resistance contribution of the corresponding electrochemical processes.[43, 44] The relaxation times (τ) associated with these RC elements represent processes such as electronic conductivity ($\tau = 1E^{-8}$–$1.5E^{-6}$), contact between the active particle and the current collector ($\tau = 2E^{-6}$–$1E^{-4}$),

View Article Online
DOI: 10.1039/D6TA03125K

cathode-electrolyte interface (τ = 1E^{-4}–0.01), charge transfer within the electrode (τ = 0.01–10), respectively.[32, 43] The overall peak area of ATC/MnHCF-3 in Figure 5 (d) is significantly lower than that of MnHCF-0 (Figure 5 (c)), indicating the faster dynamics. More precisely, the contact resistance between active particle and Al foil (τ = 2E^{-6}–1E^{-4}) in MnHCF-0 coin-cell increased largely during discharging. In contrast, the contact resistance in ATC/MnHCF-3 coin-cell (red arrows) increased mostly at high voltages, and recovered back to initial intensity at the end of discharge, proving the reversible electrochemical reaction. Moreover, the cathode-electrolyte interface (τ = 1E^{-4}–0.01) and charge transfer within the electrode (τ = 0.01–10) in MnHCF-0 coin-cell increased significantly during discharging. The increase of cathode-electrolyte interface (τ = 1E^{-4}–0.01) may be attributed to the production of by-products of side-reactions. And the increase of charge transfer resistance (τ = 0.01–10) is a result of the intercalation of lots of Na$^+$ ions.[45] In comparison, the increase of the cathode-electrolyte interface (τ = 1E^{-4}–0.01) and charge transfer within the electrode (τ = 0.01–10) in ATC/MnHCF-3 coin-cell is smaller than that in MnHCF-0 coin-cell, indicating less severe cathode-electrolyte interface (CEI) formation in ATC/MnHCF-3 electrodes.

Figure 5(e, h) indicates the Nyquist curves of MnHCF-0 and ATC/MnHCF-3 half-cells before and after 1000 cycles at 3C. Comparing with the initial Nyquist curves, the shape of the MnHCF-0 curve changed significantly after cycling, indicating a significant increase in CEI and charge-transfer resistance.[31] In contrast, the Nyquist curve of ATC/MnHCF-3 coin-cell after cycling maintained only one semicircle in 591 Ω and an oblique line, thus the increase of resistance in ATC/MnHCF-3 coin-cell is smaller than that in MnHCF-0, demonstrating the stable CEI after surface modification. Subsequently, these coin-cells were disassembled to characterize the morphology and crystal structures of electrodes by SEM and XRD methods. As depicted in Figure 5 (g, j), cracks were prevalent on the surface of the MnHCF-0 microcubes, while the ATC/MnHCF-3 particles maintain their intact cubic structure. The XRD patterns of cycled electrodes are shown in Figure S11, indicating that both MnHCF-0 and ATC/MnHCF-3 electrodes were transformed into the monoclinic phase after long-term cycling. From a crystallographic perspective, the crystal parameters of the monoclinic

View Article Online
DOI: 10.1039/D6TA03125K

phase are larger than those of the rhombohedral phase, demonstrating that repeated insertion/extraction of Na^+ ions and redox reactions of iron/manganese can ultimately lead to changes in the crystal structure. The identified structural evolution of the cathode materials provides valuable insights for the rational design and further optimization of Prussian White cathodes through crystal structure engineering. Combining in-situ EIS and post-cycling SEM measurements, we further verify that ammonium persulfate surface modification of the Prussian White microcubes is beneficial to their long-cycle stability and slows down the increase in CEI and electron transfer resistance. To sum up, the introduction of conductive carbon particles establishes efficient electronic pathways among Prussian White cubes, thereby improving charge transport. Meanwhile, surface modification serves as a protective barrier that suppresses parasitic reactions at the electrode/electrolyte interface, effectively inhibiting the dissolution of active metal species and slowing the rate of capacity decay.

View Article Online
DOI: 10.1039/D6TA03125K

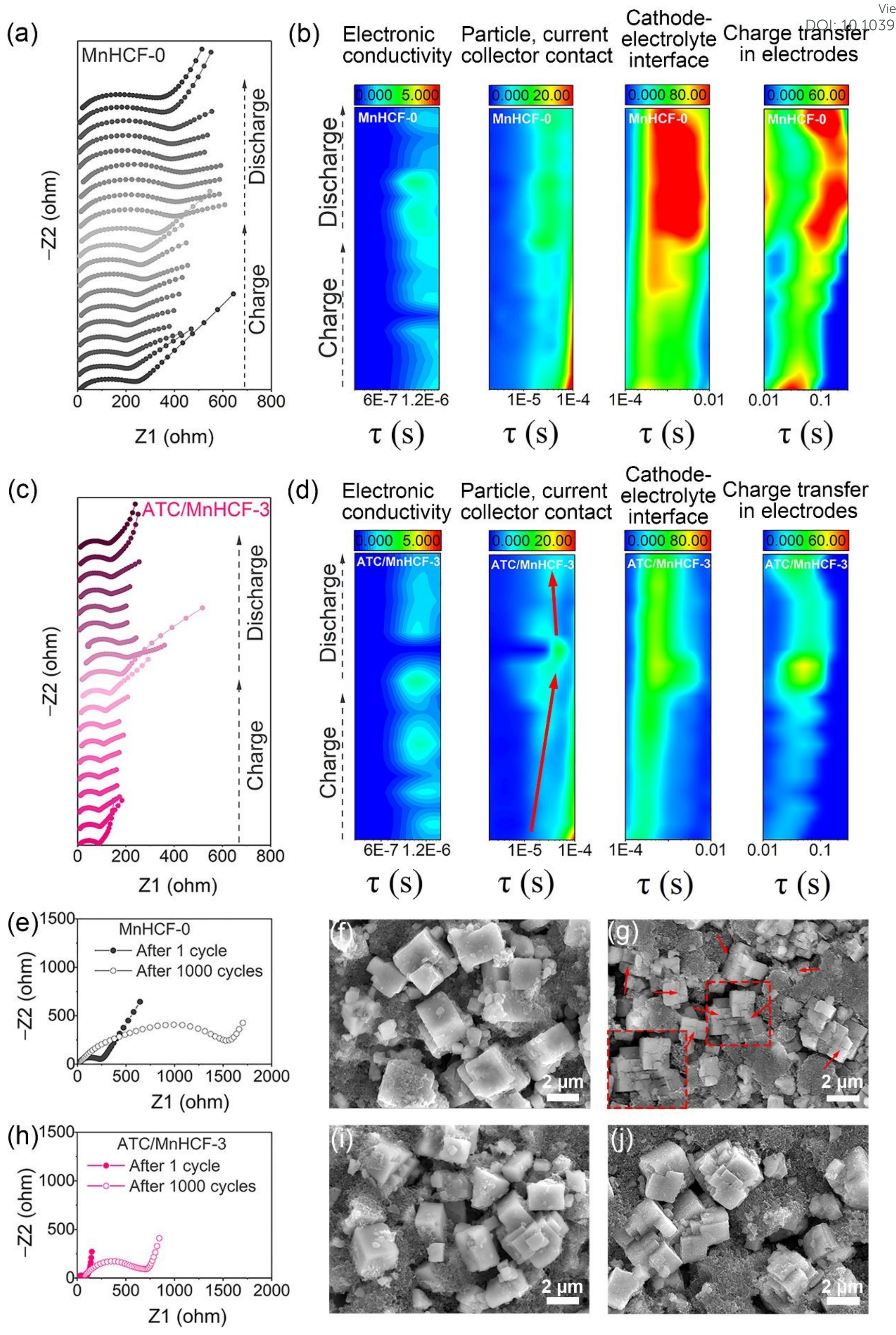

Figure 5 In-situ EIS spectra and corresponding DRT results of (a, b) MnHCF-0//Na and (c, d) ATC/MnHCF-3//Na half-cells. Nyquist plots of (e) MnHCF-0//Na and (h) ATC/MnHCF-3//Na half-cells before and after 1000 cycles at 3C. SEM images of (f,

View Article Online
DOI: 10.1039/D6TA03125K

g) MnHCF-0 and (i, j) ATC/MnHCF-3 electrodes before and after 1000 cycles at 3C.

2.5 Performance of small particles from high-concentration synthesis

To further evaluate the robustness and practical applicability of the proposed surface engineering strategy, high-concentration synthesis was performed to produce high-yield MnHCF (denoted as HY MnHCF-0). The detailed synthesis method is shown in the experimental section. In Figure 6(a), the SEM image of HY MnHCF-0 displayed agglomeration of smaller cubes in the size of 1–2 μm, reflecting the high nucleation density under concentrated reaction conditions. In Figure 6(b), the HY MnHCF-0 coin-cell demonstrated a high specific capacity of 146.7 mA·h·g^{-1} at 0.1C, illustrating that the increased specific surface area and shortened diffusion path of the small primary particles were beneficial for Na^+ transport. However, in Figure 6(c), the HY MnHCF-0 coin-cell maintained 63% of the initial specific capacity at 1C after 300 cycles. The long-term cycling data with error bars are presented in Figure S12. Although HM MnHCF-0 delivers high initial capacity due to its increased surface area, its cycling stability remains unsatisfactory. In contrast, the ATC and surface modification methods were also applied to obtain the HY ATC/MnHCF-3 sample. In Figure 6(d), the SEM image of HY ATC/MnHCF-3 showed a uniform distribution of carbon particles and microcubes. The agglomeration of microcubes was reduced due to well-dispersed carbon particles. In comparison, the initial specific capacity of HY ATC/MnHCF-3 is 140 mA·h·g^{-1} at 0.1C, and it maintained a high specific capacity of 103.5 mA·h·g^{-1} after 300 cycles at 1C. Impressively, the HY ATC/MnHCF-3 half-cell also showed a high specific capacity of 108.6 mA·h·g^{-1} at 10C in Figure 6(e, f), proving the excellent rate performance. Therefore, this surface modification strategy is broadly applicable to Prussian White cathode materials and effectively enhances their cycling stability in SIBs. Compared with the energy density and cycle life of Prussian blue analogue cathodes reported in the literature in Table S4, the HY ATC/MnHCF-3 cathode delivers a high energy density of up to 472 Wh·kg^{-1}, while maintaining a working life of approximately 600 hours. Moreover, the ATC/MnHCF-3 sample demonstrates an ultra-long operational lifetime of up to 1000 hours. These results demonstrate that the

View Article Online
DOI: 10.1039/D6TA03125K

proposed surface chemical-state engineering strategy is not limited to ideal laboratory-scale materials but remains highly effective under high-yield, high-surface-area synthesis conditions, highlighting its strong potential for practical sodium-ion battery applications.

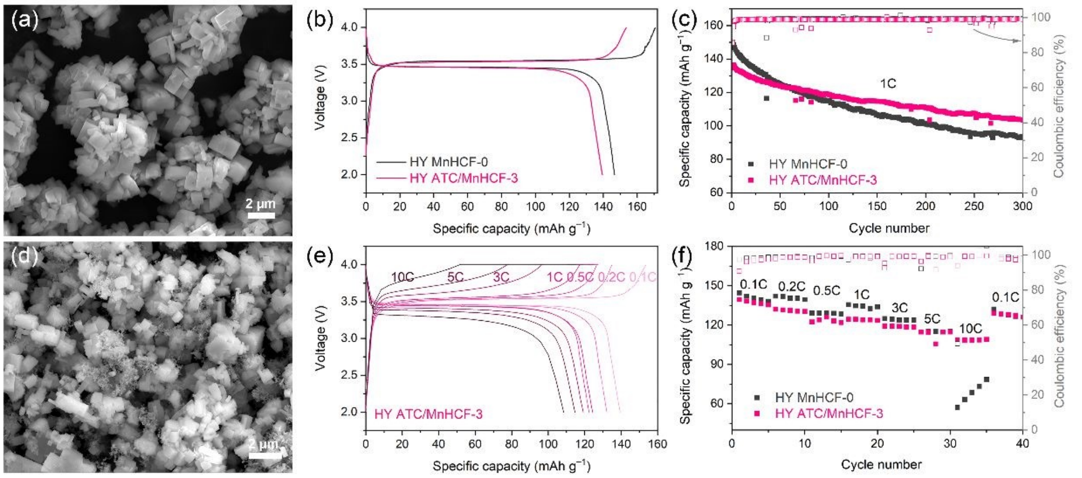

Figure 6 SEM images of (a) HY MnHCF-0 and (d) HY ATC/MnHCF-3. Electrochemical performance of HY MnHCF-0//Na and HY ATC/MnHCF-3//Na half-cells. (b) The charge and discharge curves at 0.1C. (c) Comparison of cycling performance at 1C. (e) Charge and discharge curves of the HY ATC/MnHCF-3//Na half-cell at various current densities. (f) Comparison of rate performance.

3. Conclusions

In summary, a synergistic strategy combining surface modification with acid-treated carbon additives was developed to enhance the cycling stability of MnHCF in SIBs. MnHCF-0, ATC/MnHCF-1, ATC/MnHCF-3, and ATC/MnHCF-5 were synthesized via a controlled slow coprecipitation method. Through the strong oxidizing action of ammonium persulfate, a fraction of low-spin Fe^{2+} was selectively converted into low-spin Fe^{3+} with the insertion of NH_4^+, forming protective surface layers of the modified samples. The intercalation of NH_4^+ partially reduces the amount of coordinated water in the framework. And the Fe^{3+} and NH_4^+ enriched surface layer effectively stabilized the open framework and suppressed cathode-electrolyte interface resistance during the long-term cycling. As a result, modified electrodes demonstrated markedly improved

View Article Online
DOI: 10.1039/D6TA03125K

capacity retention in sodium-ion half-cells, with ATC/MnHCF-3 delivering a high initial capacity of 115.3 mA·h·g^{-1} at 3C and sustaining excellent stability over 1000 cycles. In the further exploration of the practical implementation of manganese hexacyanoferrate, HY ATC/MnHCF-3 also delivered a high specific capacity of 140 mA·h·g^{-1} at 0.1C and an excellent rate performance (108.6 mA·h·g^{-1} at 10C). These findings highlight the crucial role of surface protection in advancing the long-term durability of Prussian White cathodes. The simple and feasible one-step surface modification method further advances the application of Prussian White cathode material in SIBs.

View Article Online
DOI: 10.1039/D6TA03125K

4. Experimental Section

4.1 Materials synthesis

Preparation of MnHCF-0

MnHCF-0 was synthesized by the coprecipitation method with a little modification. First of all, 6 mmol $Na_2MnC_{10}H_{12}N_2O_8$ ($Na_2MnEDTA$) and 6 mmol $Na_4Fe(CN)_6 \cdot 10H_2O$ were dissolved in 120 mL ultrapure water to obtain solution A, and 12 mmol ascorbic acid was dissolved in 60 mL ultrapure water to obtain solution B. Both solutions were under magnetic stirring and nitrogen protection. Then solution B was injected into solution A at a rate of 0.5 $mL \cdot min^{-1}$. The reaction solution A was always maintained at an ice bath. After the injection, the reaction solution was stirred for 1 hour and aged for 6 hours. Afterwards, the white precipitates were washed with ultrapure water and ethanol three times and finally dried at 150 °C for 24 hours in a vacuum oven.

Preparation of ATC/MnHCF-1, ATC/MnHCF-3, and ATC/MnHCF-5

First of all, 50 mg acid-treated carbon (ATC) was dispersed in 120 mL ultrapure water and was continuously ultrasonicated for 30 minutes. Then, 6 mmol $Na_2MnEDTA$ and 6 mmol $Na_4Fe(CN)_6 \cdot 10H_2O$ were added to the ATC solution (A) under magnetic stirring and an ice bath. Next, the ascorbic acid solution (B) was injected into solution A at a rate of 0.5 $mL \cdot min^{-1}$. After the injection, the reaction solution was stirred for 1 hour and aged for 6 hours. Afterwards, 10 mL precooled $(NH_4)_2S_2O_8$ solution (0.1 mmol, 0.3 mmol, and 0.5 mmol) was added into above reaction solution at a rate of 1 $mL \cdot min^{-1}$ and stirred overnight. Finally, the dark gray precipitates were washed with ultrapure water and ethanol three times and finally dried at 150 °C for 24 hours in a vacuum oven.

Preparation of high-yield MnHCF-0 and ATC/MnHCF-3

To obtain high-yield MnHCF-0 (HY MnHCF-0) and ATC/MnHCF-3 (HY ATC/MnHCF-3), it was needed to increase the mole number of $Na_2MnC_{10}H_{12}N_2O_8$ ($Na_2MnEDTA$), $Na_4Fe(CN)_6 \cdot 10H_2O$, and ascorbic acid to 12 mmol, respectively. In

View Article Online
DOI: 10.1039/D6TA03125K

addition, it was also necessary to increase the stirring time to 5 hours and the aging time to 12 hours. The entire preparation process, along with other experimental parameters, was maintained exactly as previously described.

4.2 Characterization methods

The particle morphology was characterized by Scanning Electron Microscopy (SEM, Thermofisher Quattro S ESEM microscope). The crystal structure of the synthesized materials was revealed by the X-ray diffraction method (XRD, Bruker D8 Advance powder diffraction system), followed by refinement using Fullprof software. The chemical formula of materials was calculated based on the results of Inductively Coupled Plasma Mass Spectrometry (ICP-MS, NexION 2000 PerkinElmer). The content of crystal water of samples was determined by Thermogravimetric analysis (TGA, TA Instruments Q5000) under a nitrogen atmosphere from room temperature to 600 °C at a heating rate of 10 $°C·min^{-1}$. Fourier-Transform Infrared Spectroscopy (FTIR) was performed using the Thermo Scientific Nicolet iS20 within a wavenumber of 400–4000 cm^{-1}. Raman spectroscopy was performed using a Renishaw inVia Raman microscope with an excitation wavelength of 532 nm. The valence distribution of elements was conducted by X-ray Photoelectron Spectroscopy (XPS) on Physical Electronics 5000 VersaProbe II.

4.3 Electrochemical measurements

CR2025-type coin-cells were assembled to test the electrochemical performance of the synthesized materials in a glove box. The active materials, conductive carbon (Ketjen black EC-300J) and polyvinylidene fluoride (PVDF) binder in a weight ratio of 7:2:1, were uniformly dispersed in the N-Methyl-2-pyrrolidone solvent to obtain a slurry and then were coated onto aluminum foils before being dried in a vacuum oven at 150 °C. The active material mass loading of electrodes is 1–1.5 $mg·cm^{-2}$. The electrolyte was 1M $NaPF_6$ dissolved in diglyme. Coin-cells were charged and discharged on a Land CT2001A battery testing system at room temperature within a voltage window of 2–4 V. A formation cycle at 0.1C was conducted before subsequent electrochemical testing.

View Article Online
DOI: 10.1039/D6TA03125K

The constant current 1C equals 150 mA·g^{-1}. Long-term cycling was performed using a constant-current/constant-voltage (CCCV) protocol at 1C/3C. Specifically, the cell was charged under a constant current to a cutoff voltage of 4.0 V, followed by a constant-voltage step until the current decreased to 0.01 mA, after which a standard constant-current discharge was applied. Cyclic voltammetry (CV) and Electrochemical impedance spectroscopy (EIS) were performed using a Gamry 600+. CV measurements were scanned at 0.1 mV·s^{-1} between 2 and 4 V. The frequency range of EIS measurements was set from 10^6 to 0.1 Hz.

CRediT authorship contribution statement

Tingting Yang: Conceptualization, Validation, Methodology, Data curation, Writing – original draft. **Ethan Boutelle:** Conceptualization, Methodology, Data curation, Writing – review & editing. **Maurice Efroza:** Methodology, Validation. **Penghao Zhang:** Validation, Data curation. **Peng Bai:** Conceptualization, Supervision, Writing – review & editing, Funding acquisition.

Declaration of competing interest

The authors declare that they have no known competing financial interests or personal relationships that could have appeared to influence the work reported in this paper.

Acknowledgments

This work is partially supported by National Science Foundation grants (Award No. 2044932 and No. 2431923), a McKelvey Collaboration Initiation Grant (CIG) from Washington University, and a Research Gift from TSVC. The material characterization experiments were partially supported by IMSE (Institute of Materials Science and Engineering) at Washington University in Saint Louis. The authors thank Rajeev Gopal for helpful discussions.

View Article Online
DOI: 10.1039/D6TA03125K

Reference:

1. A. Yao, S. M. Benson, and W. C. Chueh, *Nat. Energy*, 2025, **10**, 404–416.
2. F. Zhang, B. He, Y. Xin, T. Zhu, Y. Zhang, S. Wang, W. Li, Y. Yang and H. Tian, *Chem. Rev.*, 2024, **124**, 4778–4821.
3. Y. Wang, J. Yan, B. Xie, Y. Meng, C. Fu, F. Kong, X. Wang, Q. Zhou, X. Chen, J. Li, C. Du, L. Wang and P. Zuo, *Nat. Commun.*, 2025, **16**, 10083.
4. J. E. Zhou, Y. Li, X. Lin and J. Ye, *Nanomicro Lett.*, 2024, **17**, 9.
5. Z. Liang, F. Tian, G. Yang and C. Wang, *Nat. Commun.*, 2023, **14**, 3591.
6. B. Bornamehr, V. Presser, A. J. G. Zarbin, Y. Yamauchi and S. Husmann, *J Mater. Chem. A*, 2023, **11**, 10473–10492.
7. Y. Shang, B. Ren, R. Wu, J. Lin, X. Li, J. Shen, D. Yan and H. Y. Yang, *Small*, 2025, **21**, e2408018.
8. P. Hong, C. Xu, C. Yan, Y. Dong, H. Zhao and Y. Lei, *ACS Energy Lett.*, 2025, **10**, 750–778.
9. A. Clavelin, D. L. Thanh, I. Bobrikov, M. Fehse, N. E. Drewett, G. A. Lopez, D. Saurel and M. Galceran, *ACS Mater. Lett.*, 2024, **6**, 5208–5214.
10. Z. Zhou, Y. Qian, X. Chen, J. Chen, X. Zhou, W. Kuang, X. Shi, X. Wu, L. Li, J. Wang and S. Chou, *Adv. Funct. Mater.*, 2024, **34**, 2404938.
11. Z. Li, Y. Wang, F. Rabuel, M. Deschamps, G. Rousse, O. Sel and J.-M. Tarascon, *Energy Storage Mater.*, 2025, **76**, 104118.
12. H. Zhang, J. Li, J. Liu, Y. Gao, Y. Fan, X. Liu, C. Guo, H. Liu, X. Chen, X. Wu, Y. Liu, Q. Gu, L. Li, J. Wang and S. L. Chou, *Nat. Commun.*, 2025, **16**, 2520.
13. R. Wu, B. Ren, X. Wang, J. Lin, X. Li, J. Zheng, H. Y. Yang and Y. Shang, *Adv. Funct. Mater.*, 2024, **35**, 2418018.
14. F. Peng, L. Yu, P. Gao, X.-Z. Liao, J. Wen, Y.-s. He, G. Tan, Y. Ren and Z.-F. Ma, *J Mater. Chem. A*, 2019, **7**, 22248–22256.
15. Z. Xu, F. Chen, Y. Li, Y. Lu, A. Zhou, J. Jiang, X. Xu, J. Tu, B. Pan, F. Chen, Y. Huang, X. Zhao and J. Xie, *Adv. Sci.*, 2024, **11**, e2406842.
16. S. Ali, J. Jiang, C. Guo, D. Wang, X. Wang, W. Xia, M. Fu, Z. Yuan, W. Yan,

View Article Online
DOI: 10.1039/D6TA03125K

J. Li, Y. Zhang and A. Zhou, *Electrochim. Acta*, 2025, **521**, 145920.

17. Z. Zhang, Y. Gao, J. Gao, W. Si, X. Sun, F. Zhao, Y. Zhang, Z. Zhang, D. Song and J. Wu, *Chem. Commun.*, 2024, **60**, 5703–5706.
18. C. Misiewicz, A. E. Ulander, T. Melin, A. Hall and E. J. Berg, *Adv. Mater. Interfaces*, 2024, **12**, 2400854.
19. W. Shu, J. Li, G. Zhang, J. Meng, X. Wang and L. Mai, *Nanomicro Lett.*, 2024, **16**, 128.
20. B. Zhou, Y. Gao, X. Lin, B. Yang, N. Kang, Y. Qiao, H. Zhang, L. Li and S. Chou, *Chem. Sci.*, 2025, **16**, 13594–13628.
21. M. Ye, S. You, J. Xiong, Y. Yang, Y. Zhang and C. C. Li, *Mater. Today Energy*, 2022, **23**, 100898.
22. W. C. Chen, S. J. Li, H. Y. Xu, S. H. Xu and G. T. Fei, *ChemPhysChem*, 2024, **25**, e202300960.
23. Y. Jiang, L. Shen, H. Ma, J. Ma, K. Yang, X. Geng, H. Zhang, Q. Liu and N. Zhu, *J Power Sources*, 2022, **541**, 231701.
24. K. Lin, Z. He, L. Shen, J. Su, Z. Huang, Y. Xia and Y. Wang, *J. Electroanal. Chem.*, 2024, **966**, 157785.
25. X. Xu, Y. Lan, B. Zhang, S. Zhu, Y. Yang and Y. Gao, *Electrochim. Acta*, 2023, **471**, 143375.
26. M. Chen, X. Li, Y. Yan, Y. Yang, Q. Xu, H. Liu and Y. Xia, *ACS Appl. Mater. Interfaces*, 2022, **14**, 1092–1101.
27. H. Fu, X. P. Wang, J. Yang, Z. Q. Wu, H. Ren, J. N. Ji, M. J. Shi and E. H. Ang, *Chem. Sci.*, 2026*,* **17**, 968–976.
28. H. Fu, J. Yang, Z. Q. Wu, H. Ren, J. N. Ji, C. Y. Li, M. J. Shi and E. H. Ang, *J Colloid Interface Sci.*, 2026, **704**, 139331.
29. J. Song, L. Wang, Y. Lu, J. Liu, B. Guo, P. Xiao, J. J. Lee, X. Q. Yang, G. Henkelman, and J. B. Goodenough, *J Am. Chem. Soc.*, 2015, **137**, 2658–2664.
30. I.-H. Jo, S.-M. Lee, H.-S. Kim and B.-S. Jin, *J. Alloy. Compd.*, 2017, **729**, 590–596.
31. Y. Gao, H. Zhang, J. Peng, J. Wang, X. Liu, L. Zhang, Y. Xiao, L. Li, Y. Liu,

View Article Online
DOI: 10.1039/D6TA03125K

Y. Qiao, J. Wang and S. Chou, *Adv. Mater.*, 2025, **37**, e2417876.

32. Y. Wang, J. Liu, N. Jiang, J. Yang, C. Yang and Y. Liu, *Small*, 2024, **20**, e2403211.
33. Q. Liu, F. Ye, K. Guan, Y. Yang, H. Dong, Y. Wu, Z. Tang and L. Hu, *Adv. Energy Mater.*, 2022, **13**, 2202908.
34. Z. Zhao, W. Zhang, M. Liu, D. Wang, X. Wang, L. Zheng, X. Zou, Z. Wang, D. Li, K. Huang and W. Zheng, *Energy Environ. Mater.*, 2022, **6**, e12342.
35. M. Oliver-Tolentino, M. M. Gonzalez, H. Osiry, G. Ramos-Sanchez and I. Gonzalez, *Dalton Trans.*, 2018, **47**, 16492–16501.
36. L. Wang, Y. Lu, J. Liu, M. Xu, J. Cheng, D. Zhang and J. B. Goodenough, *Angew. Chem. Int. Ed.*, 2013, **52**, 1964–1967.
37. W. Wang, X. Zhu, T. Qin, Z. Pei, Z. Xu, J. Bi, J. Yin, T. Li, X. Guo and J. Lu, *Nano Energy*, 2025, **143**, 111285.
38. X. Ding, Q. Zhou, Z. Wang, L. Liu, Y. Wang, T. Song, F. Wu and H. Gao, *J Mater. Chem. A*, 2024, **12**, 27598–27609.
39. Y. Li, K. H. Lam and X. Hou, *ACS Appl. Energy Mater.*, 2021, **4**, 13098–13109.
40. M. Choi, D. Kim, Y. Y. Song, J. Seo, M. H. Kim, E. Kim, S. Ryu, D. H. Seo, A. Choi and H. W. Lee, *ChemSusChem*, 2025, **18**, e202500564.
41. X. Huang, C. Yang and Y. You, *ACS Appl. Energy Mater.*, 2022, **5**, 8123–8131.
42. X. Dong, H. Wang, J. Wang, Q. Wang, H. Wang, W. Hao and F. Lu, *Molecules*, 2023, **28**, 7267.
43. W. Fu, G. Wang, K. Zhang, J. Zheng, C. Zhang, J. Wang, J. Li, J. Zheng, M. Zhang and Z. Shen, *J Power Sources*, 2025, **641**, 236866.
44. Z. Wang, Y. Wang, B. Py, A. Maradesa, J. Liu, T. H. Wan, M. Saccoccio and F. Ciucci, *ACS Electrochem.*, 2025, **1**, 2680–2689.
45. K. R. Ren, L. Chen, C. Z. Liu, Y. Tian, X. Y. Leng, M. N. Jiang, Z. Han, G. Y. Xiao, G. N. Xu, Z. Yu, P. F. Wang, Y. Xie, Y. B. He and T. F. Yi, *Adv. Mater.*, 2025, **37**, e2507960.

View Article Online
DOI: 10.1039/D6TA03125K

Surface modification enables long-term cycling of Prussian white in sodium-ion batteries

Tingting Yang[a], Ethan Boutelle[a], Maurice Efroza[b], Penghao Zhang[a], Peng Bai[a,b,*].

[a]Department of Energy, Environmental and Chemical Engineering, Washington University in St. Louis, St. Louis, Missouri 63130, United States of America

[b]Institute of Materials Science and Engineering, Washington University in St. Louis, St. Louis, Missouri 63130, United States of America

Corresponding Author: Peng Bai

Email: pbai@wustl.edu

Data availability statements

The data supporting this article have been included as part of the Supplementary Information.